Biophysical Journal Volume 108 May 2015 2235–2248

Article

Single Cell Wall Nonlinear Mechanics Revealed by a Multiscale Analysis of AFM Force-Indentation Curves

Simona Digiuni,[1] Annik Berne-Dedieu,[2] Cristina Martinez-Torres,[1] Judit Szecsi,[2] Mohammed Bendahmane,[2] Alain Arneodo,[1] and Françoise Argoul[1,*]

[1]Centre National de la Recherche Scientifique UMR5672, Laboratoire de Physique, Ecole Normale Supérieure de Lyon, Université de Lyon I, France; and [2]Centre National de la Recherche Scientifique UMR5667, Laboratoire de Reproduction et de Développement des Plantes, Ecole Normale Supérieure de Lyon, Université de Lyon I, France

ABSTRACT Individual plant cells are rather complex mechanical objects. Despite the fact that their wall mechanical strength may be weakened by comparison with their original tissue template, they nevertheless retain some generic properties of the mother tissue, namely the viscoelasticity and the shape of their walls, which are driven by their internal hydrostatic turgor pressure. This viscoelastic behavior, which affects the power-law response of these cells when indented by an atomic force cantilever with a pyramidal tip, is also very sensitive to the culture media. To our knowledge, we develop here an original analyzing method, based on a multiscale decomposition of force-indentation curves, that reveals and quantifies for the first time the nonlinearity of the mechanical response of living single plant cells upon mechanical deformation. Further comparing the nonlinear strain responses of these isolated cells in three different media, we reveal an alteration of their linear bending elastic regime in both hyper- and hypotonic conditions.

INTRODUCTION

A plant cell wall is a composite polymeric structure made of very stiff and high-persistence-length cellulose microfibrils coated with heteroglycans (hemicelluloses such as xyloglucan), which are themselves embedded in a dense, hydrated matrix of various neutral and acidic polysaccharides with protein scaffolds. This maintains the cell wall's cohesion (1–3). Although mammalian cells also have a cross-linked actin network cortex that coats the internal plasma membrane and acts as a physical barrier for the penetration of sharp cantilevers, a much wider variety of mechanical properties can be achieved by plant cells as related to the tissue function and its environment. For instance, creep, stress relaxation, and hysteresis of load-retract curves all reflect the complex viscoelastic behavior of plant cell walls, apart from the fact that this property may also gradually change from inside to outside, depending on the aging of the cell (4). The morphology and growth behavior of a plant cell is driven by the hydrostatic turgor pressure that pushes and stretches the wall by way of its cellulosic matrix relaxation. Typical turgor pressures in plants are ~0.3–1.0 MPa, which is a range that translates to between 10 and 100 MPa of tensile stress in the walls (5). This tensile stress within the wall is a function of the cell curvature, the wall thickness H_w, and the pressure drop across the wall (6). Different methods have been designed over the past decades to characterize the single-cell-wall elastic modulus through global compression (7,8) or bending strain (9) experiments. The mechanical properties of single plant cells were also tracked down locally, with nanotipped indentation systems provided by an atomic force microscope (AFM) (10–17) or by cellular force microscopes (18,19).

The mechanical characterization of a single plant cell with an AFM cantilever depends on the tip shape. As for animal cells, large spherical indenters are better suited to capture the internal pressure of the cell, whereas sharp conical or pyramidal tips are more appropriate for characterizing the local mechanics of the wall (15,17). This latter tip geometry has been chosen in this work to study single-cell-wall mechanics from *Arabidopsis thaliana* root calli. Working with single plant cells of small size makes AFM measurements trickier for two reasons (15): the first one is due to the very low adhesion and spreading of these cells on solid surfaces traditionally used for animal cells. The second one is the lack of knowledge of both cell-wall thickness and tension in single cells. Moreover, classical analysis of AFM force curves requires a good determination of the contact point at the surface of the cell—not always easy to achieve. To help solving these issues, we develop here an original wavelet-based analysis of the force-indentation curves that reveals a succession of power-law mechanical responses encountered by the AFM cantilever during the cell penetration by the cantilever tip. These power-law responses include an intermediate regime of interest that accounts for the wall stretching and/or bending from which we can extract information about cell-wall thickness and tension. We show that this wavelet-based analysis does

Submitted June 23, 2014, and accepted for publication February 12, 2015.

*Correspondence: fargoul@ens-lyon.fr

Editor: Jennifer Curtis.

0006-3495/15/05/2235/14 $2.00

http://dx.doi.org/10.1016/j.bpj.2015.02.024

not need the knowledge of the contact point to efficiently capture nonlinear departures from the expected linear behavior for an elastic shell of a turgescent cell. Beyond investigating the statistical distributions of the cell-wall effective tension and maximum sustainable stress upon penetration, we also develop a much deeper insight on the mechanics of single plant cells, comparing turgescent cells with hypo- and hyperosmotic culture media cells. It appears from these experiments that when the turgor pressure is reduced (hypertonic medium), the wall tension decreases and even if the whole cell shape seems to be conserved, the cell-wall mechanics is damaged. When increasing the turgor pressure (hypotonic medium), the stretching of the cell wall also changes its viscoelastic response, splitting the mechanical response into two new regimes, below and above the original scaling regime that was observed with turgescent cells. Both hyper- and hypotonic media produce a decrease of single-cell effective tension. We further show that the cell-wall mechanical responses vary dramatically from cell to cell and from point to point on single cells, and we illustrate this inhomogeneous distribution on the surface of these cells by cellulose fluorescence staining.

MATERIALS AND METHODS

Single cell preparation

Single cells were separated from undifferentiated calli derived from *A. thaliana Wassilewskija* (WS-2) 35S GFP-MBD (green fluorescent protein microtubule binding domain marker) plants (14,20). Calli were grown on 4.4 g/L of MSARI-modified medium (Murashige & Skoog media with vitamins, Cat. No. M0222), 30 g/L of sucrose (Cat. No. S08069), KOH, and plant agar (Cat. No. P1001) from Duchefa Biochemie, Amsterdam, The Netherlands; and 500 mg/L of MES (Cat. No. M8250), 0.5 mg/L of 2,4D (Cat. No. D7299), 2 mg/L of IAA (Cat. No. I2886), and 7 g/L 2iPRiboside (Cat. No. D7257) from Sigma-Aldrich (Saint-Quentin Fallavier, France), pH 5.8 at 25°C and transferred every 15–20 days. Three-to-four callus pieces were placed in MS solution containing 4.4 g/L of Murashige & Skoog media with vitamins (Cat. No. M0222) and 30 g/L sucrose (Cat. No. S0809) from Duchefa Biochemie (Haarlem, The Netherlands), and 500 mg/L of MES (Cat. No. M8250; Sigma-Aldrich), pH 5.8 with KOH. After 4 h of constant agitation at 200 rpm, the cells were filtered with a 100-μm nylon mesh. The cells in MS solution were then allowed to settle down on petri dishes precoated with poly-L-lysine (50 μg/mL) and placed under the AFM microscope. Once isolated from their tissues, these cells acquire different morphologies, transitioning from spherical to tubular shapes. For the purpose of analysis, we preferentially selected cells with spherical shapes (Fig. 1 *a*) and performed the force-indentation experiments at the cell centers to prevent a lateral slipping while indenting. To generate hyperosmotic stress, 1 mL of a 1 mol/L mannitol solution was added to 5 mL of MS solution containing the cells to produce the cell plasmolysis. On the opposite, hypoosmotic stress was generated by the addition of 2 mL water to 5 mL of MS solution containing the cells.

Atomic force microscopy

Force curves on isolated cells were recorded with two different systems: a Bioscope Catalyst (Bruker, Palaiseau, France and Coventry, UK) mounted on a fluorescent macroscope and a CellHesion 15–200-μm motorized stage (JPK Instruments, Berlin, Germany) mounted on an inverted microscope in contact mode. We used model No. MPP-12220 triangular shape cantilevers with a nominal spring constant of $k = 5$ N/m (Bruker) with a sweeping velocity of 1 μm/s. Force curves recorded on the bottom of a petri dish containing the MS solution were used to calibrate the deflection sensitivity of the cantilever in liquid. The effective spring constant k of these cantilevers was estimated in between 2 and 3 N/m by directly recording their free fluctuations in MS solution, computing their power spectrum distribution, and fitting these curves with Lorentzian distributions (21–23).

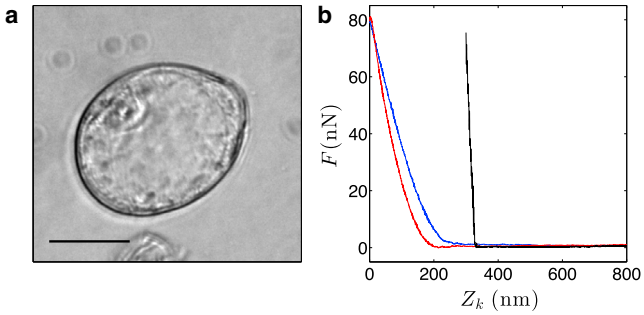

FIGURE 1 (*a*) Bright-field microscopy of a single cell from *A. thaliana* root callus; the scale bar is 25 μm. (*b*) Untreated force curves recorded in liquid on the bottom of a petri dish (*black line*) and on a single cell: (*blue line*) loading force curve; (*red*) unloading curve. The slope of the black line corresponds to the cantilever spring constant k; this slope k is used to correct the force curves (see text). To see this figure in color, go online.

Force-displacement curves were reconstructed from AFM cantilever deflection signals recorded during the decrease of the vertical position Z_k of the cantilever with respect to the sample surface Z_s. When the tip of the cantilever comes precisely into cell contact without being deflected (zero contact force), $Z_k = Z_{k0}$. Once the cell is deformed by the cantilever $Z_k < Z_{k0}$, the difference $\Delta Z_k = Z_{k0} - Z_k$ is given by the sum of the cell deformation $\delta_C = h_{C0} - h_C$ and the ratio of the force F over the cantilever spring constant k (24) as

$$Z_{k0} - Z_k = h_{C_0} - h_C + F/k. \quad (1)$$

A typical set of force curves (approach curve in *blue* and retraction curve in *red*) is shown in Fig. 1 *b*. On the right side of these curves, the cantilever is not yet in contact with the cell, so the force F does not change. When the cantilever comes into contact with the cell surface, the force curve abruptly changes its curvature and increases progressively as the cell is deformed by the penetration of the cantilever tip. The nominal spring constant of the cantilever ($k = 5$ nN/nm) was chosen large enough for the cantilever deflection to be small compared to the cell deformation. This is illustrated by the black force curve in Fig. 1 *b* recorded on a stiff glass coverslip, it corresponds to the correction term $\delta_k = F/k$ in Eq. 1. The loading (*blue*) and unloading (*red*) force curves do not overlap in Fig. 1 *b*, suggesting a partial viscous-loss during this single cell indentation (12,13,25). This slight discrepancy of loading and unloading force curves has been observed in all experiments performed in this work. In the sequel of this article, we will exclusively focus on the loading force curves.

We collected 3457 force curves from 92 *A. thaliana* cells in three different media (60 cells in MS solution, 20 cells in MS solution + mannitol and 12 cells in MS solution + water). We checked that the cantilever stiffness was chosen adequately to be much larger (at least three times) than the cell rigidity. All the curves were corrected, taking into account the cantilever stiffness. When the range of the indentation length (Z_k) was <150 nm, we kept the force curves with a large enough (>0.3 in $\log_{10} s\omega_0$) scaling domain for the computation of the β-exponent (obtained by plotting $T_{g(2)}[F](Z_{kM}, S)$ along the WT maxima line $Z_{kM}(s)$, as described below).

Confocal microscopy

Single cells in MS solution were stained using Pontamine Fast Scarlet 4B (Aldrich Rare Chemicals Library S479896; Sigma-Aldrich,) according to Anderson et al. (4). GFP and Pontamine Fast Scarlet 4B signals were detected using a model No. LSM700 confocal microscope (Zeiss, Jena, Germany) equipped with a 488-nm laser (to detect GFP signal) and a 555-nm laser (to detect Pontamine fast scarlet signal). Z-confocal series were recorded using a 40× water immersion objective and a 500-nm step size. The images and the three-dimensional z-stack projection were analyzed using the software IMAGEJ (National Institutes of Health, Bethesda, MD).

RESULTS

A wavelet-based method to analyze force-indentation curves

The continuous wavelet transform (WT) is a mathematical technique introduced in signal analysis in the 1980s (26). Since then, it has been the subject of considerable theoretical developments and practical applications in many domains (27–31). In particular in the context of this study, the WT has been applied to characterize AFM images of rough surfaces (32) and to image living cells via diffraction phase microscopy (33). It has proved very efficient to estimate scaling exponents and multifractal spectra (34–38). Within the norm $\mathscr{L}^1$, the one-dimensional WT of a signal $F(x)$ reads

$$W_\psi[F](b,s) = \frac{1}{s}\int_{-\infty}^{\infty} F(x)\psi^*\left(\frac{x-b}{s}\right)dx, \tag{2}$$

where b is a position and s (>0) is a scale parameter (see the Supporting Material for further explanation).

The interest of the WT method is twofold. The first advantage is to use the same smoothing function to filter out the experimental background noise and to compute first- and second-order derivatives with the same smoothing characteristic scale. The second advantage relies on the powerfulness of the WT to detect singularities in a signal (29,30,34,35) and to quantify their force via the estimate of the local Hölder exponent from the behavior across scales of the WT modulus maxima (WTMM) (29–31,34–38). If the wavelet has a compact support, it is straightforward to show that the WT of F, $W_\psi[F](x_0, s)$, depends upon the values of $F(x)$ in a neighborhood of x_0 of size proportional to the scale s. More generally, for any admissible analyzing wavelet ψ, one can show that if $F(x)$ behaves as $(x - x_0)^h$ in the neighborhood of x_0, then the WT of F behaves as a power law of the scale with the exponent h (34,35):

$$\left|W_\psi[F](x_0,s)\right| \propto As^h. \tag{3}$$

This relation defines how $|W_\psi\ [F](x_0, s)|$ decays when the scale s goes to zero. From the WT, we can therefore recover the local Hölder exponent of the function F, via a simple linear regression fit in a logarithmic representation.

In this study, we use modified versions of the definition (Eq. 2) of the WT that give directly a measure of F in nanoNewtons, dF/dZ in nN/nm and d^2F/dZ^2 in Pascal, once smoothed by a Gaussian window ($g^{(0)}(x)$) of width s,

$$T_{g^{(0)}}[F](b,s) = W_{g^{(0)}}[F](b,s), \tag{4}$$

$$T_{g^{(1)}}[F](b,s) = \frac{1}{s}W_{g^{(1)}}[F](b,s), \tag{5}$$

$$T_{g^{(2)}}[F](b,s) = \frac{1}{s^2}W_{g^{(2)}}[F](b,s), \tag{6}$$

where $g^{(1)}(x)$ and $g^{(2)}(x)$ are the first- and second-order derivatives of $g^{(0)}(x)$ (Supporting Material). Then the local power-law exponent extracted from the WT (Eq. 3) is shifted by -1 or -2, for the first- and second-order derivatives, respectively:

$$T_{g^{(i)}}[F](x_0,s) \propto As^{h-i}. \tag{7}$$

For illustration, let us consider a piecewise linear function F (Fig. 2 *a*):

$$\begin{aligned} F(Z_k) &= \alpha Z_k \quad \text{for } Z_k < Z_0, \\ F(Z_k) &= 0 \quad \text{for } Z_k \geq Z_0, \end{aligned} \tag{8}$$

with $\alpha > 0$. This function is continuous, but its first derivative is discontinuous (jumping from α to 0) at $Z_k = Z_0$ and its second derivative is a Dirac delta distribution. In Fig. 2 are

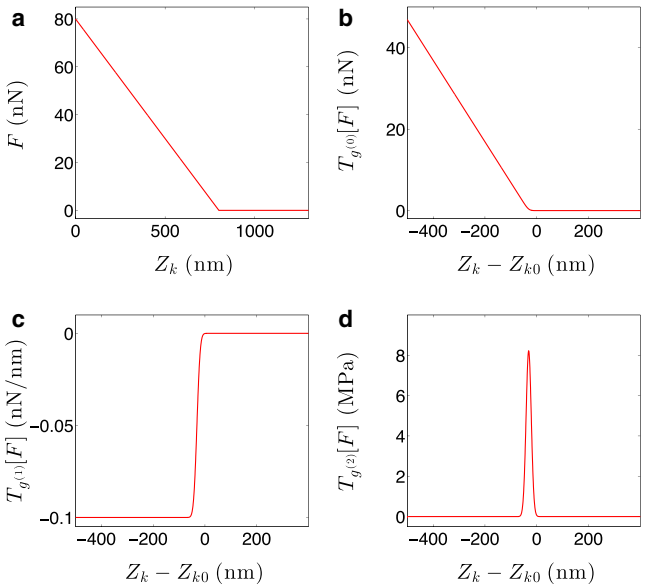

FIGURE 2 Computation of the first and second derivatives of a piecewise linear function using the WT method with a Gaussian function ($sw_0 = 10$ nm). (*a*) The original force curve. (*b*) $T_{g(0)}[F](Z_k - Z_{k0}, s = 1)$, where Z_{k0} corresponds to $T_{\text{contact}} = 10^{-4}$ nN/nm (see text). (*c*) $T_{g(1)}[F](Z_k - Z_{k0}, s = 1)$ in nN/nm. (*d*) $T_{g(2)}[F](Z_k - Z_{k0}, s = 1)$ in MPa. To see this figure in color, go online.

illustrated the two WTs of F computed at the scale $s = 1$ in a $w_0 = 10$ nm unit, using Eqs. 5 (Fig. 2 *c*) and 6 (Fig. 2 *d*), respectively. The value w_0 is a constant value that corresponds to the minimum wavelet size used in this study ($s = 1$). The jump in the first derivative of F and the sharp peak (Dirac) in the second derivative of F at $Z_k = Z_0$ are smoothed by the Gaussian of width $sw_0 = 10$ nm. In this theoretical example, we perfectly know the contact point $Z_{k0} = Z_0$, which is a crucial issue in experimental situations. Indeed the determination of Z_{k0} is a major limitation that groups working on AFM have been facing for more than a decade in their interpretations of experimental noisy force-indentation curves (14,15,39–43). The wavelet-based analysis that we propose here allows us to overcome this difficulty, by simultaneous smoothing out the noise and thresholding the force curve slope $T_{g(1)}[F](Z, s = 1)$ at the value T_{contact} beyond the contact defined at Z_{k0}:

$$T_{g^{(1)}}[F](Z_{k0}, s = 1) = T_{\text{contact}}. \quad (9)$$

For the piecewise linear model in Fig. 2, we used $T_{\text{connect}} = -10^{-4}$ nN/nm, leading to a value of Z_{k0} slightly above Z_0 because the center of the jump in $T_{g(1)}[F]$ in Fig. 2 *c* and the position of the peak in $T_{g(2)}[F]$ in Fig. 2 *d* are slightly shifted toward negative $Z_k - Z_{k0}$ values.

To estimate the Hölder exponent of F at the discontinuity point Z_{k0} of dF/dZ, we simply need to plot $T_{g(2)}[F](Z_{kM}, s)$ along the WT maxima line $Z_{kM}(s)$ (Fig. 3). Fig. 3 *a* shows the color-coded image of $T_{g(2)}[F](b,s)$ in the (b,s) half-plane, together with the so-called maxima line (plotted in *red*) defined by the WTMM obtained at each scale s (34,35). Along the maxima line, we should recover the predicted scaling law $T_{g(2)}[F](Z_{kM}, s) \propto s^{\beta}$ with $\beta = h - 2 = -1$ (Eq. 7). This is verified in Fig. 3 *c*, when plotting $T_{g(2)}[F](Z_{kM}, s)$ versus sw_0 in a logarithmic representation where, by linear regression fit, we get an estimate of the exponent $\beta = -1.002 \pm 0.005$, consistent with the theoretical prediction for a Dirac delta distribution. The scaling law $T_{g(2)}[F](Z_{kM}, s) \propto s^{-1}$ is actually observed over the whole range of scales $10 < sw_0 < 800$ nm. Let us point out that when fitting instead $\log_{10} T_{g(0)}[F](Z_{k0} - Z_k)$ versus $\log_{10}[Z_{k0} - Z_k]$ as commonly performed in the literature (39,41), we do not recover correctly a slope $h = +1$ due to the sensitivity of this curve to the choice of the contact point Z_{k0}. For instance, taking Z_{k0} such that $|T_{g(1)}[F](Z_{k0}, s = 1) = -10^{-4}|$ nN/nm (Fig. 3 *b*), we do not get nice scaling and the expected $h = +1$ exponent is only guessed at very large indentations. Because the WTMM method amounts to tracing the local singularity across scales without a priori knowledge of the contact point Z_{k0}, where the maxima line is expected to converge in the limit $s \to 0^+$, and without any need of precisely defining this contact point, it proves to be very efficient to estimate quantitatively the local Hölder exponent $h = \beta + 2 = 1$ (Fig. 3 *c*).

WTMM characterization of force-indentation curve models

Description of typical AFM force curves

Four force curves captured with the AFM on single plant cells isolated from *A. thaliana* calli are shown in Fig. 4 *a*. In this example, we have selected four different responses taken from two cells (*green* and *red*) at two different positions (*continuous* and *dotted-dashed lines*) to underline the inter- and intracellular variability that we have commonly observed in our single plant cell experiments. Similarly to the piecewise linear model in Fig. 2 *c*, when increasing indentation, the first derivative of these force curves (Fig. 4 *c*), computed with Eq. 5 for $sw_0 = 10$ nm, decreases sharply from zero to reach a plateau. The flatter this plateau, the closer the Hölder exponent to 1. The occurrence of a plateau means that there is a whole range of Z values where $F(Z)$ behaves linearly. When this plateau occurs, its value $T_{g(1)}[F] = -k_E$ provides an estimate of an effective tension of the cell wall in nN/nm (the dimension of a surface stress) at the measurement point. However, for most cells, there is not a strictly constant plateau of $T_{g(1)}[F]$, so we have used instead the second derivative of F to compute an effective stiffness parameter for these cells. Within the linear response theory, k_E is proportional to E (the wall Young modulus) times the wall thickness H_w. The width and the height of the jump from zero to this plateau varies from cell to cell but also with the position of the indentation point on a given cell. The widening of the jump in $T_{g(1)}[F]$ is

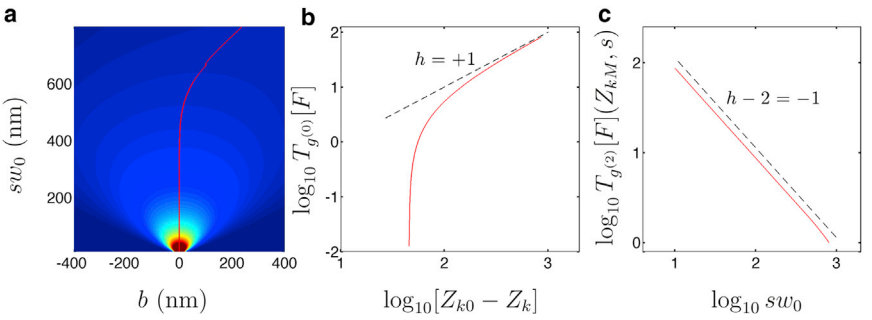

FIGURE 3 (*a*) WT representation $T_{g(2)}[F]$ of the piecewise linear function shown in Fig. 2 *a*. The color map is chosen from 0 (*dark blue*) to 2 MPa (*dark red*). (*Red line*) WT modulus maxima. (*b*) $\text{Log}_{10} T_{g(0)}[F](Z_{k0} - Z_k)$ versus $\log_{10}[Z_k - Z_{k0}]$. (*Dashed line*) Slope $h = +1$. (*c*) Plot of $\log_{10} T_{g(2)}[F](Z_{kM}, s)$ versus $\log_{10}(sw_0)$, on the WT modulus maxima line. (*Dashed line*) Slope $\beta = h - 2 = -1$. To see this figure in color, go online.

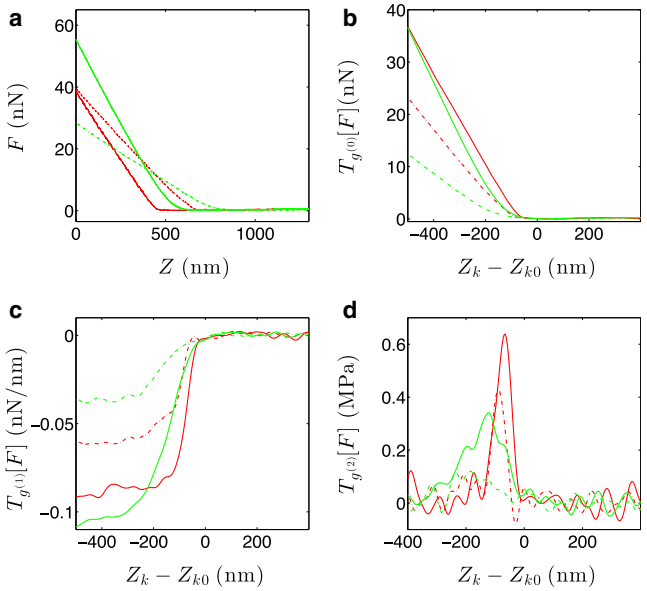

FIGURE 4 Experimental force curves (approach) collected on two different cells. (*a*) Force-indentation curves. (*b*) Plot of $T_{g(0)}[F]$ versus $Z_k - Z_{k0}$. The value Z_{k0} corresponds to $T_{\text{contact}} = -10^{-3}$ nN/nm (Eq. 9). (*c*) Plot of $T_{g(1)}[F]$ versus $Z_k - Z_{k0}$. (*d*) Plot of $T_{g(2)}[F]$ versus $Z_k - Z_{k0}$. (*Continuous* and *dotted-dashed red curves*, *continuous* and *dotted-dash green curves*, respectively) The same cell, but taken with the AFM tip at different positions. The smoothing scale is $s = 1$ ($sw_0 = 10$ nm). To see this figure in color, go online.

correlated to the penetrability of the cell wall by the tip. It can be quantified by looking at $T_{g(2)}[F]$ versus $Z_k - Z_{k0}$ (Eq. 6) (Fig. 2 *d*), which displays a peak positioned at the contact point whose (half) width gives an indication of the thickness of the cell wall and its height quantifies the maximum sustainable pressure upon penetration of the wall by the cantilever tip. We can therefore recover an effective wall stiffness with the product of the local maxima of $T_{g(2)}[F]$ times the scale at which it is estimated. Because the wall has a finite thickness, and because its mechanical strength may vary during its indentation, following this peak along the WTMM maxima line from large to small scales (Fig. 3 *a*) will allow us to evidence and quantify locally changes in the wall effective stiffness k_E. According to the wall thickness, the range of indentations of the wall will be smaller or larger and the maximum sustainable wall indentation will be attained earlier or later. From Fig. 4, *c* and *d*, we therefore conclude that the wall of the cell coded in dotted-dashed green is softer than the one of the cell coded in dotted-dashed red, and the continuous green curve suggests that the wall thickness penetrated by the tip is ~100 nm (half the width of the jump).

Models of mechanical responses of a walled-cell

During its progression into the cell, the sharp pyramidal tip of the AFM cantilever penetrates first into the cell wall with a minor modification of its curvature (Regime A, Fig. 5 *a*)

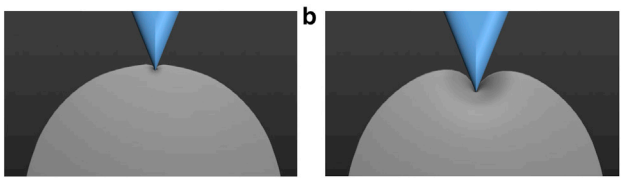

FIGURE 5 Sketch of the indentation of the cell wall by a pyramidal shape tip. (*a*) The tip penetrates the wall without noticeably changing its curvature (Regime A). (*b*) For a deeper indentation, the wall curvature is modified by the pyramidal tip (Regime B). To see this figure in color, go online.

and then bends the cell wall, acting on a thin viscoelastic shell (Regime B, Fig. 5 *b*). For a given deflection of the cantilever (the contact force), the total displacement of the AFM piezo transducer is the sum of the cantilever deflection $\delta_k = F/k$, the depth of penetration of the tip inside the wall δ_p, and the deformation (change of curvature) of the wall δ_b. We use the first derivative of the force curve, computed with the wavelet transform and Eq. 1, to subtract the cantilever deflection term and recover a simple equation for the total indentation δ_C of the cell:

$$\delta_C(F) = [Z_{k_0} - Z_k]_{\text{corr}} = \delta_p(F) + \delta_b(F). \qquad (10)$$

Regime A: penetration of the cantilever tip inside the cell wall (*shallow indentations*). The relation $\delta_p(F)$ depends on the shape of the cantilever tip. With the pyramidal shape cantilevers used in this work, we must consider two regimes for the tip penetration inside the wall because the tip is not infinitely sharp and has a finite curvature radius r_t. Roughly speaking, when the indentation is limited to $\delta_p \lesssim r_t$, the shape of the tip can be approximated by a hemisphere and when the indentation increases beyond r_t ($\delta_p \gtrsim r_t$), the cantilever must rather be considered as a square pyramid. These two geometries give force-indentation power laws known, respectively, as Hertz (44) and Sneddon (45) equations.

For $\delta_p \lesssim r_t$ (Hertz),

$$F(\delta_p) = \left[\frac{4E\sqrt{r_t}}{3(1-\nu^2)}\right]\delta_p^{3/2}. \qquad (11)$$

In the limit $\delta_p >> r_t$ (Sneddon), and assuming that $\delta_p < H_w$,

$$F(\delta_p) = \left[\frac{\tan(\theta)E}{\sqrt{2}(1-\nu^2)}\right]\delta_p^2, \qquad (12)$$

where E is the Young modulus of the wall, ν is the Poisson ratio, and θ is half the tip angle. These formulae predict that if the wall is soft enough for being penetrated by the cantilever tip, we should first observe a power law $\delta^{3/2}$ followed by a power law δ^2, assuming that the wall is thick enough ($H_w >> r_t$). A complete solution of the transition from sphere to pyramid has already been reported in

Rico et al. (46). Because the wall has a finite thickness H_w, the first power law $F(\delta_p) \sim {\delta_p}^{3/2}$ is more likely observed in the experiments.

Regime B: global deformation of the cell wall (*stretching and bending*). Assuming that the wall thickness is <1/10 the cell radius, the theory of spherical shells predicts a linear behavior for $F(\delta_b)$, when the wall Young modulus can be considered as homogeneous in space and invariant during the deformation (47–49). Here we will consider a more general form for $F(\delta_b)$ with a nonlinearity exponent h that will generalize these linear response models to strain-hardening ($h > 1$) or strain-softening ($h < 1$) systems,

$$F(\delta_b) = k_E\, \delta_b^h, \tag{13}$$

where k_E can be considered as an effective tension of the wall.

Piecewise nonlinear model mimicking a force-indentation curve. To guide the interpretation of the experimental force curves, we have generalized the piecewise model discussed above (Eq. 8), to a nonlinear model including a first local penetration regime ($F(\delta_p) \propto {\delta_p}^{3/2}$) and a large-scale deformation regime ($F(\delta_b) \propto {\delta_p}^{h}$):

$$\begin{aligned} F(Z_k) &= 0 && \text{for } Z_k \geq Z_0, \\ F(Z_k) &= A(Z_k - Z_0)^{3/2} && \text{for } Z_1 < Z_k < Z_0 : \text{Regime A}, \\ F(Z_k) &= k_E(Z_k - Z^*)^h && \text{for } Z_k < Z_1 : \text{Regime B}. \end{aligned} \tag{14}$$

The values of A, Z^*, and $F(Z_1)$ are determined as functions of the parameters k_E (effective wall tension or stiffness) and $Z_1 - Z_0$ (wall thickness), by fulfilling the continuity of F and of its first derivative at Z_0 and Z_1. In consistency with the values measured in the experiments reported in Fig. 4, we set $k_E = 0.1$ nN/nm and $Z_0 - Z_1 = 100$ nm. We show in Fig. 6 the three (orders 0, 1, and 2) derivatives of F computed with a smoothing Gaussian wavelet at the scale $s = 1$ with $w_0 = 10$ nm, for three Hölder exponent values: $h = 1.2$ (*green curve*), 1 (*red curve*), and 0.8 (*brown curve*). The occurrence of a plateau in $T_{g(1)}[F]$ (*red curve* in Fig. 6 *c*) at large indentations means that the bending deformation δ_b of the cell wall prevails over the wall tip penetration length δ_p. The curves corresponding to other Hölder exponents differ only in the deformation regime B, because we keep the same term for the penetration regime A (-100 nm $< Z_k - Z_{k0} < 0$). The first-order derivative of F is continuous at $Z_k = Z_1$ but its second-order derivative is discontinuous; the smaller the exponent h, the larger the jump in $T_{g(2)}[F]$ at this transition point Z_1. For $h < 1$, this second derivative abruptly changes its sign when crossing Z_1. Even if the experimental force curves shown in Fig. 4 were selected among the $h > 1$ class responses, we have also observed many cell responses corresponding to $h < 1$.

In this ad hoc model (Eq. 14), we have assumed that the wall deformation is nonlinear for large indentations, which includes the possibility of changes of the cell-wall tension during its deformation. Fitting the force curves to recover the underlying scaling laws is again sensitive to the choice of the contact point. As shown in Fig. 7 *b* for the two force curves of Fig. 6 *a* corresponding to $h = 1$ (*red curve*) and $h = 1.2$ (*green curve*), depending on our choice of the contact point Z_{k0}, the representation of the force curve function in logarithmic scales may be more or less convincing. We choose two different origins Z_{k0} to compute the variable $\delta = |Z_k - Z_{k0}|$ to illustrate the high sensitivity of the reconstruction of these curves (corresponding, respectively, to $T_{\text{contact}} = -10^{-4}$ nN/nm for the *solid curves* and $T_{\text{contact}} = -10^{-3}$ nN/nm for the *dashed curves*). We note that the exponents $h = 1$ and 1.2 can be recognized for indentation $\delta = Z_{k0} = Z_k$ larger than 100 nm, whereas the penetration regime ($\delta^{3/2}$) (Eq. 14) is also visible over a decade $\delta \leq 100$ nm. However, decreasing slightly the contact point Z_{k0} shortens dramatically the range of indentation values where the 3/2 exponent can be estimated. With this noiseless theoretical case, we realize that if, for instance, the threshold criteria on T_{contact} were relaxed further, the shape of the $\log_{10} T_{g(0)}[F](Z_k - Z_{k0}, s = 1)$ curve beyond Z_1 would no longer be fittable by a straight line, meaning that the estimation of the exponent h would become intractable.

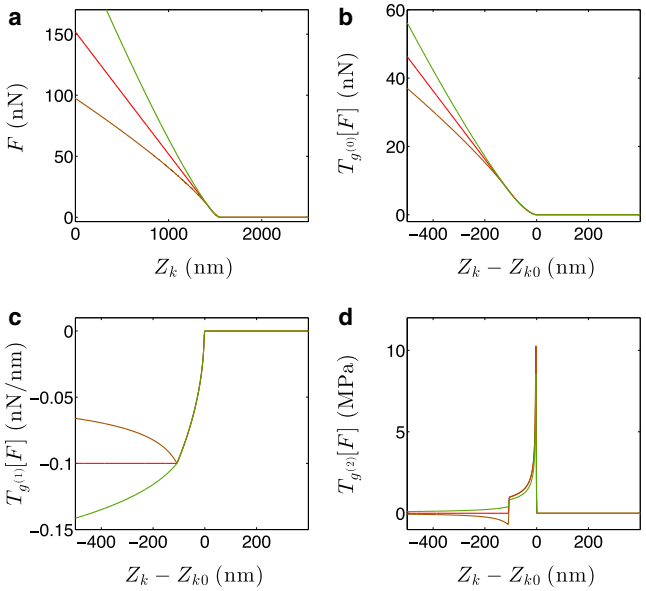

FIGURE 6 Computation of the first and second derivatives of the nonlinear force-curve model (Eq. 14) using the WT method with a Gaussian function ($sw_0 = 1$ nm with $w_0 = 1$ nm). (*Green*, *red*, and *brown curves*) Hölder exponents $h = 1.2$, 1, and 0.8, respectively. (*a*) The original force curves. (*b*) $T_{g(0)}[F](Z_k - Z_{k0}, s = 1)$, Z_{k0} corresponds to $T_{\text{contact}} = -10^{-4}$ nN/nm (see text). (*c*) $T_{g(1)}[F](Z_k - Z_{k0}, s = 1)$ in nN/nm. (*d*) $T_{g(2)}[F](Z_k - Z_{k0}, s = 1)$ in MPa. To see this figure in color, go online.

Wavelet-based multiscale analysis of theoretical force curves

For comparison, Fig. 7, *a* and *c*, show the color-coded space-scale (b,s) representation of $T_{g(2)}[F](Z_k - Z_{k0}, s)$ computed from the same two theoretical force signals in Fig. 6 *a*

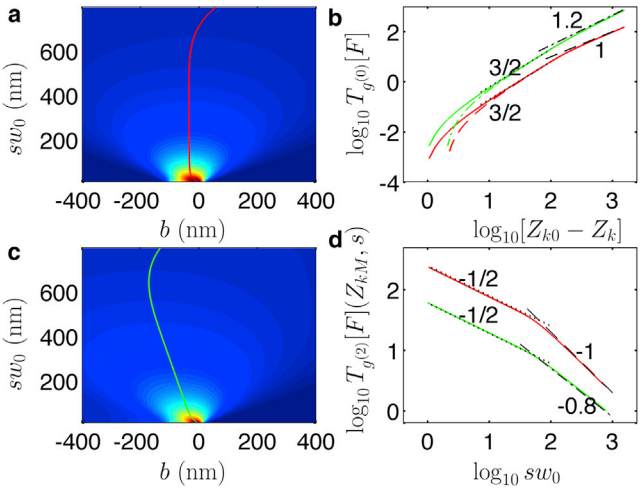

FIGURE 7 Wavelet-based analysis of two theoretical forces curves. (*a* and *c*) Color-coded representation (from 0, *dark blue* to 2 MPa, *red*) of $T_{g(2)}[F](Z_k - Z_{k0}, s)$ computed from two of the force curves in Fig. 6 *a*, corresponding to the Hölder exponents $h = 1$ (*a*) and $h = 1.2$ (*c*). The WTMM line is coded with the same color as the original force curve. (*b*) $\text{Log}_{10}T_{g(0)}[F](Z_k - Z_{k0}, s = 1)$ versus $\log(\delta) = \log(Z_{k0} - Z_k)$ with $T_{\text{contact}} = -10^{-4}$ nN/nm (*solid curves*) and $T_{\text{connect}} = -10^{-3}$ nN/nm (*dashed curves*). (*Black-dashed*, *dashed-dotted*, and *dotted straight lines*) Slopes 1, 1.2, and 3/2 corresponding to the scaling behavior $F \propto \delta$, $F \propto \delta^{1.2}$, and $F \propto \delta^{3/2}$, respectively. (*d*) Logarithmic representation of $T_{g(2)}[F]$ versus scale sw_0 along the WT maxima lines shown in (*a*) and (*c*). (*Black dashed*, *dotted-dashed*, and *dotted straight lines*) Scaling behavior of $T_{g(2)}[F] \propto s^{-1}$, $s^{-0.8}$, and $s^{-1/2}$, respectively. To see this figure in color, go online.

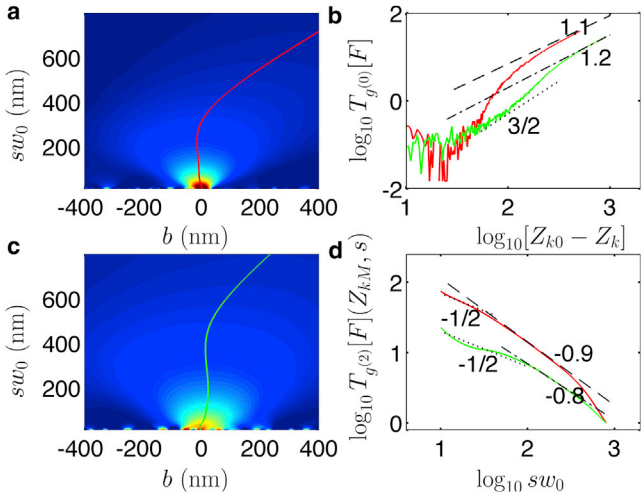

FIGURE 8 Wavelet-based analysis of two experimental force curves. (*a* and *c*) Color-coded representation (from 0, *dark blue* to *red*, 500 kPa (*a*) and 150 kPa (*c*)) of $T_{g(2)}[F](b,s)$ computed from two force curves of Fig. 4 *a* with the same color and line coding. (*b*) $\text{Log}(\delta) = \log_{10}T_{g(0)}[F](Z_k - Z_{k0}, s = 1)$ versus $\log(\delta) = \log(Z_{k0} - Z_k)$ with $T_{\text{contact}} = -5.510^{-3}$ nN/nm. (*Black dashed*, *dashed-dotted*, and *dotted straight lines*) Slopes 1.1, 1.2, and 3/2 corresponding to the scaling behavior $F \propto \delta^{1.1}$, $F \propto \delta^{1.2}$, and $F \propto \delta^{3/2}$, respectively. (*d*) Logarithmic representation of $T_{g(2)}[F]$ versus scale sw_0 along the WTMM lines shown in (*a*) and (*c*). (*Black dashed*, *dotted-dashed*, and *dotted straight lines*) Scaling behavior: $T_{g(2)}[F] \propto s^{-0.9}$, $s^{-0.8}$, and $s^{-1/2}$, respectively. To see this figure in color, go online.

corresponding to the exponent values $h = 1$ (*red curve*) and $h = 1.2$ (*green curve*). The local maxima line of $T_{g(2)}[F](Z_{k0} - Z_k, s)$ points toward the point Z_{kM} of maximum stress of the tip of the cantilever with the shell cortex when the scale sw_0 tends to 1 nm (in the experiments we cannot afford such a small scale, and we will limit our scale analysis to 10 nm). The color code is the same in Fig. 7, *a* and *c*; the larger the h, the larger the force for a given deformation and the weaker the divergence of $T_{g(2)}[F](Z_{k0} - Z_k, s)$ when s tends to zero. As shown in Fig. 7 *d*, not only are the large-scale power laws expected from the deformation regimes B ($T_{g(2)}[F] \propto s^{-1}$ (and $s^{-0.8}$) well recognized now, but also the scaling regime ($s^{-1/2}$) at low scales. This new wavelet-based approach allows us to recover not only the correct scaling exponents but also the whole interval of scales where these scaling laws are expected to be fulfilled. This gives us confidence in the chance to resolve these two scaling domains $s^{-1/2}$ and s^{β} with $\beta = h - 2$ (Eq. 7) in experimental situations.

Wavelet-based multiscale analysis of experimental force-indentation curves

Turgescent cells

As a first experimental application of our wavelet-based methodology, we report in Fig. 8 the results of a similar analysis of two force curves shown in Fig. 4. Note that the color-coding range of $T_{g(2)}[F](b,s)$ in Fig. 8 *a* is 3.3 times larger than in Fig. 8 *c* because the latter cell (*green line*) is softer than the former (*red line*). Similarly to the theoretical case discussed just above, we can detect a WTMM line (coded with the same color as the force curve) pointing to the maximum stress at Z_{kM} when $sw_0 \rightarrow 10$ nm. We again compare in Fig. 8, *b* and *d*, the scaling behavior of the force-indentation curves and of the WTMM along the maxima lines, respectively. The affordable scaling regime B of $T_{g(0)}[F](Z_k - Z_{k0}, s = 1)$ in Fig. 8 *b* is shifted toward larger indentations (>400 nm) for the green curve and is barely identifiable in the red curve. This distortion of the curve is typically what we anticipated in the theoretical modeling. Enhanced by the presence of noise, the practical incapacity to have a precise estimation of Z_{k0} impairs the characterization of the power-law regime. At low indentations, the shape of the red force-indentation curve misses completely the first penetration regime, and we cannot therefore have any estimation of the cross-over scale in between the low and large indentation regimes (Eq. 14). The green curve seems more favorable, because we can delineate a low indentation range with the scaling law $F \propto \delta^{3/2}$, although it is hindered by the experimental noise. Even though we suspect that this green curve behaves with a power law $F \propto \delta^{1/2}$ at larger indentations, it is again impossible to trust the cross-over indentation scale (~400 nm) where this power-law seems to arise. The analysis with the WTMM lines (Fig. 8 *d*) gives

a much clearer picture of the two indentation regimes involved in these two force curves. We have plotted dashed and dotted-dashed straight lines with slopes $\beta = -0.9$ (*red curve*) and $\beta = -0.8$ (*green curve*) to highlight the range of scales sw_0 where these power-law behavior values of $h = \beta + 2 = 1.1$ and 1.2 appear, respectively. At scales $sw_0 > 100$ nm (respectively, 65 nm) for the green (respectively, *red*) curve, the maxima line enters a power-law regime outlined with a dashed line in Fig. 8 *d*. The minimum scale where this scaling law occurs (noted as $\min(sw_0)$ in the following figures) is very important for this study, because it provides an estimate of how far the cell wall is penetrated by the tip, i.e., a measure of its softness. The experimental examples reported in Fig. 8 confirm that the WTMM method is very efficient to 1) reveal and delimit the range of scales over which scaling operates and 2) estimate the corresponding power-law exponents with good accuracy.

Practically, to compute the exponent $\beta = h - 2$ from the WTMM curves versus sw_0, we do not take a fixed range of scales. For each force curve, we first detect the largest scale range where $\log_{10}[\max(T_{g(2)}[F])1$ versus $\log_{10}(sw_0)$ can be fitted with a linear function within 1% error. Because our experimental force curves are limited in indentation depth, we restrict this scale range from above to the maximum scale $sw_0 < 400$ nm to avoid finite-size effects in the WTMM computation.

Fig. 9 *a* represents the range of sw_0 values where a linear behavior (fixed β) has been detected from a sample of single *A. thaliana* turgescent cells. The corresponding histogram of β-values shown in Fig. 9 *b* is broadly distributed around a mean value ~−0.9. We did not expect such a result because we thought that when working on single cells extracted from an undifferentiated tissue, the mechanical response would be more homogeneous, and that, for instance, the distribution of β-values would be peaked at ~−1 (corresponding to $h = 1$). Another important observation is the variability of the range of scales and more importantly of the minimum scale $\min(sw_0)$ where a power-law behavior of the WTMM can be extracted along the maxima lines (Fig. 9 *c*). Note that when β is <-1, the scaling range seriously shrinks down to half a decade, meaning that there is probably not really a scaling law in that case, but instead a global crossover from a first-penetration regime A that extends to larger depths, to a larger-scale regime B that cannot be attained because we are limited in scales. These $\beta < -1$ scaling responses correspond to $h < 1$ (Eq. 13), which is precisely to strain-softening wall domains, where the cell wall may lack cohesion in the cellulose architecture.

This large variability of the mechanical parameters of *A. thaliana* single cells led us to perform confocal fluorescence microscopy to image the distribution of cellulose on the cell cortex (Fig. 10). Fig. 10 *a* is obtained from a confocal section and shows the boundary distribution of cellulose and microtubules underneath. Fig. 10 *b* illustrates the whole surface of the cell, observed from above, where we clearly notice a nonhomogeneous distribution of cellulose. The white arrow points to a hole of cellulose, and the yellow arrows point to external cellulose deposits. If we correlate the mechanical properties of the cell wall to its cellulose content, this image conforms to the wide distribution of β-exponents measured on turgescent cells (Fig. 9 *b*). We also remark in Fig. 10 *a* that the microtubules

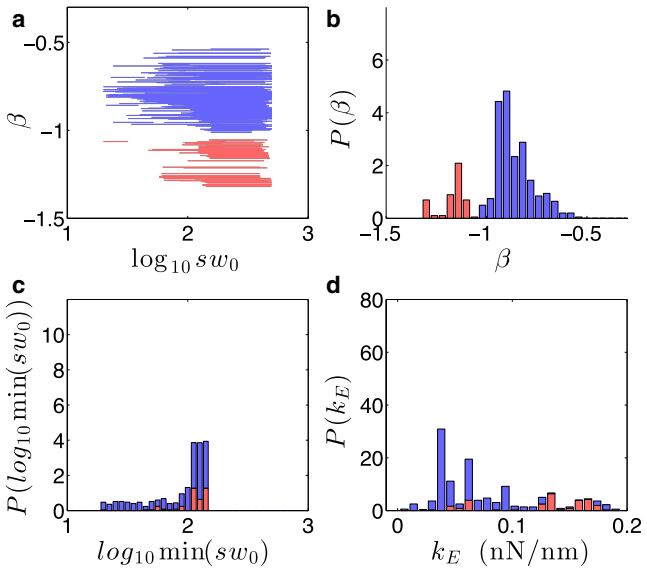

FIGURE 9 Statistical analysis of the mechanical properties of turgescent *A. thaliana* cell walls (2,111 force curves captured on 60 cells). (*a*) β-exponents plotted versus the range of scales sw_0 (in log scale). (*b*) Histogram of β-values. Two intervals of β-values are distinguished with different color codings ($\beta > -1$ ($h > 1$) in *blue*, $\beta < -1$ ($h < 1$) in *red*). (*c*) Stacked histograms of the minimum scale sw_0 (in $\log_{10}$) delimiting the scaling range from below. (*d*) Stacked histograms of effective stiffness k_E coefficient. To see this figure in color, go online.

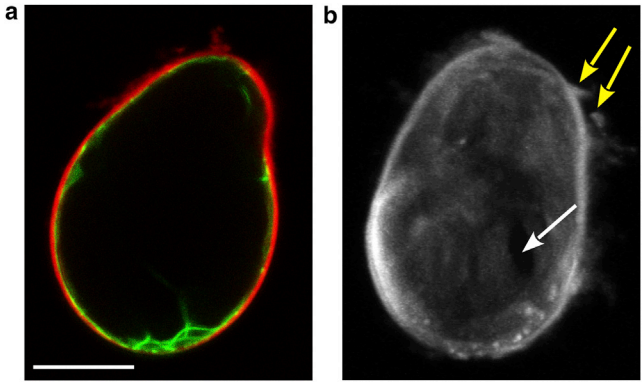

FIGURE 10 Confocal images of turgescent single *A. thaliana* cells. (*a*) Middle section of a cell expressing 35S:GFP-MBD (*green*) that marks microtubules, and stained with Pontamine Fast Scarlet 4B (*red*) that marks cellulose. (*b*) Three-dimensional z-stack projection (IMAGEJ software; National Institutes of Health) of a half cell stained with Pontamine Fast Scarlet 4B (*gray*). (*White arrow*) Region with less cellulose; (*yellow arrows*) irregularities of the cell wall. Scale bar, 20 μm. To see this figure in color, go online.

are not distributed over the periphery of this cell wall but, instead, strictly confined to it bottom part. These fluorescence images (Fig. 10) corroborate our suspicion concerning the heterogeneity in mechanical properties of turgescent plant cells.

We choose two-color-coding in Fig. 9, *a* and *b*, to distinguish β-exponents below (in *red*) and above (in *blue*) -1, and trace to which effective wall stiffness these part of the β-histograms (Fig. 9 *b*) correspond. The histograms of the effective stiffness k_E in Fig. 9 *d* show that the force curves of turgescent cells with β-exponents smaller than -1 ($h < 1$) are stiffer than those with β-exponents larger than -1 ($h > 1$). The value k_E is computed for each force curve from the second derivative modulus maximum $T_{g(2)}$ where the scaling law with exponent β is detected; this wavelet maximum modulus is then multiplied by the wavelet width at this scale to get an effective stiffness in nN/nm. Fig. 9 *d* shows that the distribution of k_E values is limited to a bounded interval, $k_E < 0.2$ nN/nm. Clearly, the upper bound of this interval of k_E values is far below the nominal spring constant of the cantilever (~5 nN/nm), suggesting that this maximum effective wall tension is a characteristic of our 60-cell sample, including eight different pools of cells. The observed variability of k_E is a strong characteristic of these cells. It results not only from variations in the Young modulus, but also from the thickness of their walls. Again the fluorescence images in Fig. 10 support this observation and suggest that the coefficient k_E commonly used to quantify the cell-wall rigidity is not the most appropriate parameter to separate the different cell domains corresponding to strain-hardening ($\beta > -1$, $h > 1$), neutral ($\beta = -1$, $h = 1$), and strain-softening ($\beta < -1$, $h < 1$) situations. Computing a standard deviation on k_E is not relevant either, because we do not have a Gaussian distribution for k_E (Fig. 9 *d*). The β-distribution above -1 bears a stronger resemblance to a Gaussian distribution (Fig. 9 *b*), which suggests that whatever the stiffness of the different wall domains may be, the ability of the cell to change its strain response during indentation (strain-softening, neutral or strain-hardening) is a better indicator of healthy turgescent cells when combined with their effective stiffness.

The histogram of β-values in Fig. 9 *b* led us to the conclusion that these single turgescent cells extracted from *A. thaliana* calli respond to a mechanical stress through a great variability of strain functions. Direct evidence on how these mechanical properties are distributed in space are obtained by mapping the cell by a grid of force curves, as shown in Fig. 11. We captured $10 \times 10 = 100$ force curves on a 10×10 μm^2 grid from a single turgescent cell (Fig. 11 *a*) and we reconstructed in Fig. 11, *b–d*, the maps of the three quantities—the Hölder exponent h, the minimum scale sw_0 delimiting the scaling range of the WTMM line from below, and the effective stiffness k_E, respectively. The map of Hölder exponents in Fig. 11 *b*

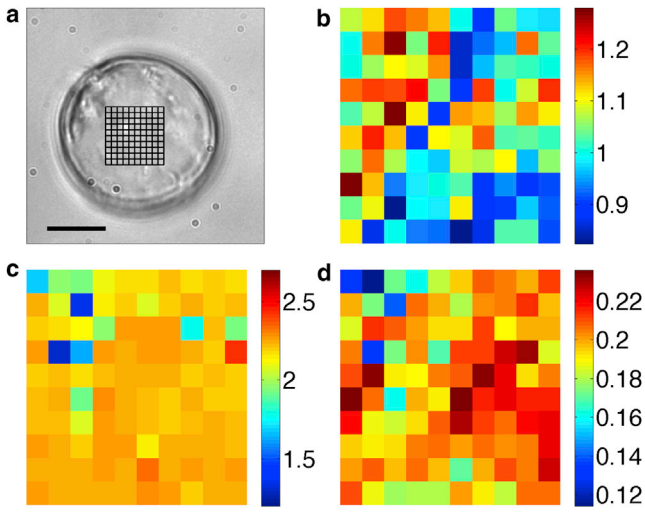

FIGURE 11 Two-dimensional maps of the three quantities $h = 2 + \beta$ (*b*), minimum scale sw_0 (in $\log_{10}$) delimiting the scaling regime s^β of the WTMM along the maxima line (*c*) and the effective wall stiffness k_E (in nN/nm) (*d*) captured from a single turgescent cell shown in (*a*). One-hundred force curves were recorded from a 10×10 μm^2 grid, superimposed to the bright-field microscopy image of this cell in (*a*). Scale bar, 10 μm. To see this figure in color, go online.

shows that this cell wall has a strong heterogeneity of strain responses, from $h = 0.8$ to $h = 1.3$, with the upper-left corner behaving rather like a strain-stiffening domain (*red* and *dark red squares*), and the diagonal of the map and the lower-right corner behaving rather like strain-softening zones (*blue squares*). In between these domains, we also have neutral strain responses (*light-green squares*). This strong variability is not reflected on the minimum scale sw_0 that serves to delimit the WTMM scaling range (Fig. 11 *c*), suggesting that the tip penetration does not change much in this example as an indication that the thickness of the wall does not vary significantly. The map of effective stiffness k_E shows two patches with higher stiffness (*dark red* > 0.2 nN/nm) separated by a diagonal line (*light green-blue*) corresponding to k_E values at ~0.18 nN/nm. The spatial distribution of k_E correlates quite well to h, large k_E values corresponding to large h values, meaning that the regions where the cell wall is stiff also have the propensity to stiffen even further upon deformation (strain-stiffening regions). On the opposite, the softer regions would have less ability to sustain the deformation (strain-softening regions). The corresponding histograms obtained from these 100 force curves can be found in Fig. S2 in the Supporting Material. From the histogram of β-values (Fig. S2 *b*), we see that this cell has a range of Hölder exponents centered at $h \simeq 1.1$ ($\beta \simeq -0.9$), with a narrower distribution than the one previously obtained in Fig. 9 *b*. The peak in the histogram of min(sw_0) in Fig. S2 *c* is much finer than in Fig. 9 *c*, and confirms that the penetration of this cell is not changing much over the considered grid surface. Finally, the distribution of wall tension k_E values is globally shifted

to higher values, and somewhat peaked in the interval 0.18–0.20 nN/nm. As already visible in Fig. 11 *d*, the variability of k_E can be considered negligible as compared to the variability of the Hölder exponent. This observation indeed makes sense because the shape of a turgescent cell is completely determined by the mechanical property of its wall. If this shape does not change rapidly in time (which is actually what we observe on the systems we are considering in this study), the wall should be locally at equilibrium and its tension should not change dramatically on the cell surface. The variability of these cell responses comes from the richness of their strain responses that ultimately would maintain a stability of the wall tension despite some local variations of the wall's Young modulus. This Young modulus would be directly proportional to the tightness and compactness of the network of cellulose fibrils.

This variability cannot be explained solely by the separation process of the tissue into single cells, performed by a gentle and smooth agitation. Fig. S3 shows a three-dimensional reconstructed confocal image of the cellulose patches of a piece of *A. thaliana* root callus. This image shows that the calli are constituted by a disorganized agglomeration of cells with a cellulose-rich matrix surrounding them. This staining confirms that, at this stage, there are already patches of cell walls with highly variable cellulose contents. This strongly suggests that the inhomogeneity of the cell wall cellulose fibrils is an intrinsic property of these undifferentiated cells, which is maintained during the cell separation process. The inhomogeneity of this living tissue makes a direct estimation of the wall thickness by electron microscopy a difficult task. Nevertheless, we succeeded in capturing scanning electron microscopy images on frozen root callus samples, untreated and unstained to avoid any alteration of their wall structure. Fig. S4 brings additional evidence of the strong variability of the wall thickness (highlighted with *colored stars*). From both these characterizing methods, we can only conclude that the wall thickness of root callus ranges in between 100 and 1000 nm. However, this estimation cannot be extrapolated to the single cells isolated from the callus tissue.

Plasmolyzed cells

To push further the mechanical characterization of these single plant cells, we have tested two different media—one with a higher osmotic pressure (addition of a polyol: mannitol) and the other with a lower osmotic pressure (dilution with water). The characterization of hyperosmotic cells is reported in Fig. 12. The range of scales where the exponent β can be retrieved with 1% error is dramatically reduced (Fig. 12 *a*). The difference with turgescent cells is impressive; the β-exponent distribution is shifted to higher β-values with a small percentage of β-values <-0.9 (Fig. 12 *b*). The $\beta < -1$ responses have completely disappeared. The fact that β is increasing beyond -0.9 is a strong indication of strain-hardening responses. Indeed the

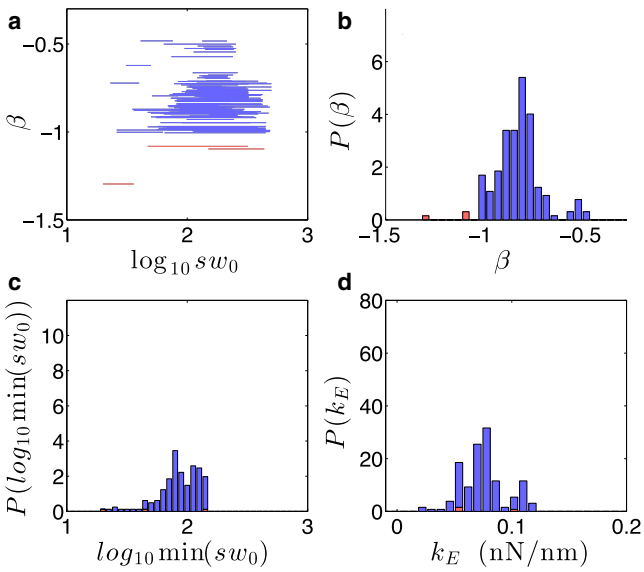

FIGURE 12 Statistical analysis of the mechanical properties of *A. thaliana* single cell walls under hypertonic conditions (900 force curves captured on 20 cells; for details, see Materials and Methods). (*a*) β-exponents plotted versus the range of scales sw_0 (in log scale). (*b*) Histogram of β-values. Two intervals of β-values have been distinguished with different color codings as in Fig. 9. (*c*) Stacked histograms of the minimum scale sw_0 (in $\log_{10}$) delimiting the scaling range from below. (*d*) Stacked histograms of effective stiffness k_E coefficient. To see this figure in color, go online.

plasmolysis of the cells changes drastically the way they adapt to a mechanical stress. The minimum scale values sw_0 are now grouped at ~100 nm (Fig. 12 *c*). The effective tension coefficient k_E is globally decreased (Fig. 12 *d*), meaning that these cells behave as softer cells. Thus, if the thickness of the wall penetrable by the tip increases, its Young modulus must decrease—likely resulting in a decrease of k_E. But this variation of k_E is not very large, and cannot be used as a good criteria for comparing turgescent from plasmolyzed cells. A more discriminating criteria turns out to be the β-exponent and the range of scales where it can be detected, which, a posteriori, contributes to validate the multiscale analysis performed with the WTMM method.

Cytolyzed cells

Finally, the characterization of cells in hypoosmotic media (Fig. 13) is also very instructive. We may consider that this hypoosmotic media pushes the internal turgor pressure to higher values, and thus increases the tension of their walls or destabilizes them if there is a local rupture. The WTMM scaling analysis brings into light an amazing result: β-values ~-0.9 (mild strain-hardening responses) are diminished whereas the probability of neutral and strain-softening responses ($\beta \in [-1.2;1]$) is increased (Fig. 13 *b*). The range of β-values is actually split in two separate β-ranges, which can be made visible on the surface of these cytolyzed cells with fluorescence staining of

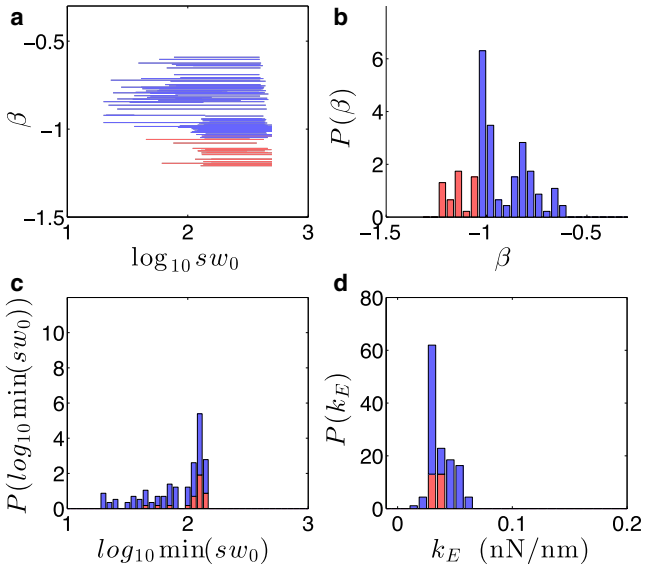

FIGURE 13 Statistical analysis of the mechanical properties of cytolyzed *A. thaliana* cell walls (446 force curves captured on 12 cells; for details, see Materials and Methods). (*a*) β-exponents plotted versus the range of scales sw_0 (in log scale). (*b*) Histogram of β-values. Two intervals of β-values have been distinguished with different color codings as in Fig. 9. (*c*) Stacked histograms of the minimum scale sw_0 (in $\log_{10}$) delimiting the scaling range from below. (*d*) Stacked histograms of effective stiffness k_E coefficient. To see this figure in color, go online.

cellulose (Fig. S5). On the one hand, there may be a reinforcement of stronger, strain-hardening domains; on the other hand, an enlargement of the weaker strain-softening domains may result from stretching-induced damage. The variability of the minimum of sw_0 for the strain-softening domains is actually wider than for turgescent cells (Fig. 13 *c*). The histogram of effective tensions k_E (Fig. 13 *d*) shows a global decrease, with a mean value ~0.03 nN/nm, with the smaller k_E values corresponding to smaller β-exponent values (strain-softening domains).

DISCUSSION

The walls of plant cells vary dramatically in their cellulose fiber composition with plant type. More recently the hierarchical structure of plant materials (3,50–52) has raised increasing interest among botanists and biologists to explain the wide range of their mechanical properties. In this article, we show that on a single plant cell, we have already a whole variety of mechanical behavior that will likely be used by the plant for further development. This high variability requires a broader view of the mechanics of shells. Let us review the energy terms involved in a shell indentation by a sharp cantilever. At shallow indentations (Regime A), the models of Hertz (Eq. 11) and Sneddon (Eq. 12) are frequently used to extrapolate the Young's modulus to characterize cell-wall stiffness in plant cells (14,15,17,53). When the tip of the cantilever penetrates further into the cell wall, a larger deformation occurs that may stretch and bend the wall on larger scales (Regime B) (Fig. 5). The stretching energy per unit surface for a homogeneous expansion of a sphere of radius R reads (54)

$$E_{\text{stretch}} \propto K_S \left(\frac{d}{R}\right)^2, \tag{15}$$

where A is the stretched surface, d is the displacement of an elementary surface, and K_S is the stretching modulus, $K_S = EH_w/(1-\nu^2)$. The bending energy per unit surface is

$$E_{\text{bend}} \propto K_B \left(\frac{d}{R^2}\right)^2, \tag{16}$$

where K_B is the bending modulus,

$$K_B = \frac{1}{12} K_S H_w^2 = EH_w^3/\left(12\left(1-\nu^2\right)\right). \tag{17}$$

The ratio of the stretching over the bending energies scales therefore as

$$\frac{E_{\text{stretch}}}{E_{\text{bend}}} \propto \left(\frac{R}{H_w}\right)^2. \tag{18}$$

When the local radius of curvature R is less than the wall thickness H_w, the bending energy is not negligible as compared to the stretching energy. We can therefore suspect that both these energies will impact the wall response. If the cell wall is very stiff (large Young modulus E), the tip of the cantilever will not penetrate very far inside the wall and the wall will instead flatten and curve on large radius R (Fig. 5 *b*), because it will cost much less to bend ($E_{\text{bend}} \propto EH_w/R^2 \times H_w^2/R^2$) than to stretch ($E_{\text{stretch}} \propto EH_w/R^2$) the wall. The first regime A will therefore be very short in penetration length, and the range of scales sw_0 for computing β will be larger. It is typically what is observed for β-exponents larger than -1 for the turgescent cells. For this set of responses, $h > 1$ means that the force implied for the cell deformation increases faster than expected for a linear response, and the deformation of the cell wall is less and less easy (strain-hardening). This may be explained by the fact that the wall texture and mechanics is not constant over its thickness, with two (or more) layers of different mechanical responses; to prevent wall deformations that are too large, the inner layer could be stiffer than the outer layer (15,50). On the other hand, if the wall Young modulus is comparatively low, the cantilever tip will penetrate deeper inside the wall, and the energy cost for bending it will be much higher than for stretching. The range of scale sw_0 where the WTMM behaves as a power law will be shifted to larger scales, and it will be more difficult to have a correct estimation of the scaling exponent β. There is a set of responses of turgescent cells that give a β-exponent smaller than -1 ($h < 1$), where the range of sw_0 is markedly diminished (both from below and above) (Fig. 9 *b*). The wall domains corresponding to these responses are probably much

softer, and their penetration by the tip is easier than expected for a linear regime; we can call them "strain-softening" domains.

Note that although the heterogeneity of the mechanical properties of plant cell walls was guessed in previous works (14,15), the presence of strain-hardening and strain-softening domains, to our knowledge, has never been remarked upon before. From the histogram of k_E values and the range of sw_0, we can give an estimation of an effective cell wall Young's modulus $E \sim k_1/\langle sw_0 \rangle$: $E \sim 0.49 \pm 0.25$ MPa for the turgescent cells, $E \sim 0.32 \pm 0.18$ MPa for the hypertonic cells, and $E \sim 0.16 \pm 0.12$ MPa for the hypotonic cells. These estimations of E are in quite good agreement with other AFM force curve studies on isolated single cells with sharp pyramidal tips (15,17). However, they are three orders-of-magnitude lower than those obtained from whole tissues such as leaves, for instance (7,16,19,53), suggesting either that the cell wall structure is very different or that beyond the wall of each cell, there are additional layers that reinforce the whole tissue to maintain its cohesion. We must also remark that the sharp tip indenter used in this work allows very local measurements that do not modify the cellulose fiber network over long distances. This can therefore explain why this local perturbation leads to much lower elastic modulus estimations. Note also that we are working with undifferentiated call cells that have not yet achieved the rigidity required by a whole tissue.

The loss of a wide β-scaling range is observed in plasmolyzed cells (hypertonic mannitol medium) (Fig. 12). These cells lose their wall bendability and elasticity, typically as inflated balls (Fig. S5, *a* and *b*). The effective tension k_E, which is related to EH_w in that case, is comparatively lower in plasmolyzed cells than in turgescent cells. If one keep computing the exponent β on a very narrow range of scales, despite the lack of convincing scaling law, its shift to larger values (closer to zero) is the signature of some further increase of the h exponent, revealing again a strain-hardening of these cells and the inhomogeneity of their wall. It is also important to note that the plasmolyzed cells lack completely the original $\beta = -1$ ($h = 1$) behavior of the turgescent cells, confirming a strong modification of their bending elasticity. Finally, when the cells are submitted to a hypotonic media (Figs. 13 and S5, *c* and *d*), their internal water pressure is increased, which strongly modifies their normal turgescent response and likely destabilizes the wall mechanics. The fact that we recover a scaling range that extends to values <100 nm (compared to plasmolyzed cells) means that these cells keep their ability to bend on large domains (as long as such large homogeneous domains exist). However, they lose the range of β-exponents in between -1 and -0.9, to keep only the strain-hardening ($\beta > -0.8$, $h > 1.2$) and the strain-softening ($\beta < -1$, $h < 0.9$) responses. Is it precisely the intermediate regime of β-values close to -0.9 (only observed in turgescent cells) that would be the most active and the easiest to remodel upon a mechanical stress? We note also in Fig. 13 *b* that, contrarily to turgescent cells, a nonnegligible fraction of cytolyzed cells behave as purely elastic shells ($\beta = -1$). Finally, the collapse of the effective stiffness k_E of cytolyzed cells could point out their progressive destabilization under higher internal turgor pressure.

CONCLUSION

We have elaborated on an original approach to study the mechanics of single plant cells, based on a multiscale decomposition of force-indentation curves collected from an atomic-force microscope. We have shown that the mechanical characteristics of living cells usually embodied in their Young moduli are not sufficient to capture the complexity of deformation response of walled-cells. It is therefore necessary to develop new methods that help understanding of the nonlinearities of these responses. The wavelet transform modulus maxima method has been adapted here to quantify these nonlinearities on single cells, isolated from *A. thaliana* calli, and examined in iso-, hyper-, or hypotonic conditions. We have shown that the well-known elastic response of plant cell walls is strongly challenged by our methodology, which reveals that only a finite percentage of cytolyzed cells can behave as purely elastic shells (bending elasticity). This study also illuminates the necessity of considering their nonlinear response via the computation of the nonlinear exponent h, providing additional information to the commonly used Young's modulus estimation. This could also help in distinguishing cell domains that have stronger remodeling ability under a mechanical stress.

SUPPORTING MATERIAL

Supporting Materials and Methods and five figures are available at http://www.biophysj.org/biophysj/supplemental/S0006-3495(15)00221-0.

ACKNOWLEDGMENTS

We are very grateful to T. Muller and A. Duprat from JPK Instruments for their exclusive support on the installation of CellHesion system in our laboratory. We also thank A. Asnacios, L. Berguiga, K. Berthet, A. Boudaoud, P. Durand-Smet, and O. Hamant for very fruitful discussions.

This work has been supported by Agence Nationale de la Recherche grants No. ANR-10-BLAN-1516, ANR 10-BLANC-1615, and ANR-11 IDEX-0007-02 with the PRES-University of Lyon.

REFERENCES

1. Fry, S. C. 2004. Primary cell wall metabolism: tracking the careers of wall polymers in living plant cells. *New Phytol.* 161:641–675.
2. Burgert, I. 2006. Exploring the micromechanical design of plant cell walls. *Am. J. Bot.* 93:1391–1401.
3. Geitmann, A. 2010. Mechanical modeling and structural analysis of the primary plant cell wall. *Curr. Opin. Plant Biol.* 13:693–699.

4. Anderson, C. T., A. Carroll, …, C. Somerville. 2010. Real-time imaging of cellulose reorientation during cell wall expansion in *Arabidopsis* roots. *Plant Physiol.* 152:787–796.
5. Wei, C., and P. M. Lintilhac. 2007. Loss of stability: a new look at the physics of cell wall behavior during plant cell growth. *Plant Physiol.* 145:763–772.
6. Carpita, N. C. 1985. Tensile strength of cell walls of living cells. *Plant Physiol.* 79:485–488.
7. Wang, C. X., L. Wang, and C. R. Thomas. 2004. Modeling the mechanical properties of single suspension-cultured tomato cells. *Ann. Bot. (Lond.).* 93:443–453.
8. Geitmann, A. 2006. Experimental approaches used to quantify physical parameters at cellular and subcellular levels. *Am. J. Bot.* 93:1380–1390.
9. Nezhad, A. S., M. Naghavi, …, A. Geitmann. 2013. Quantification of the Young's modulus of the primary plant cell wall using Bending-Lab-On-Chip (BLOC). *Lab Chip.* 13:2599–2608.
10. Arnoldi, M., C. M. Kacher, …, M. Fritz. 1998. Elastic properties of the cell wall of *Magnetospirillum gryphiswaldense* investigated by atomic force microscopy. *Appl. Phys. A Mater. Sci. Process.* 66:613–617.
11. Arnoldi, M., M. Fritz, …, A. Boulbitch. 2000. Bacterial turgor pressure can be measured by atomic force microscopy. *Phys. Rev. E Stat. Phys. Plasmas Fluids Relat. Interdiscip. Topics.* 62:1034–1044.
12. Parre, E., and A. Geitmann. 2005. More than a leak sealant. The mechanical properties of callose in pollen tubes. *Plant Physiol.* 137:274–286.
13. Parre, E., and A. Geitmann. 2005. Pectin and the role of the physical properties of the cell wall in pollen tube growth of *Solanum chacoense*. *Planta.* 220:582–592.
14. Milani, P., M. Gholamirad, …, O. Hamant. 2011. In vivo analysis of local wall stiffness at the shoot apical meristem in *Arabidopsis* using atomic force microscopy. *Plant J.* 67:1116–1123.
15. Radotić, K., C. Roduit, …, S. Kasas. 2012. Atomic force microscopy stiffness tomography on living *Arabidopsis thaliana* cells reveals the mechanical properties of surface and deep cell-wall layers during growth. *Biophys. J.* 103:386–394.
16. Forouzesh, E., A. Goel, …, J. A. Turner. 2013. In vivo extraction of *Arabidopsis* cell turgor pressure using nanoindentation in conjunction with finite element modeling. *Plant J.* 73:509–520.
17. Zdunek, A., and A. Kurenda. 2013. Determination of the elastic properties of tomato fruit cells with an atomic force microscope. *Sensors (Basel).* 13:12175–12191.
18. Yang, S., and M. T. A. Saif. 2008. Microfabricated force sensors and their applications in the study of cell mechanical response. *Exp. Mech.* 49:135–151.
19. Routier-Kierzkowska, A.-L., A. Weber, …, R. S. Smith. 2012. Cellular force microscopy for in vivo measurements of plant tissue mechanics. *Plant Physiol.* 158:1514–1522.
20. Mathur, J., and C. Koncz. 1998. Callus culture and regeneration. *Methods Mol. Biol.* 82:31–34.
21. Sader, J. E., I. Larson, …, L. R. White. 1995. Method for the calibration of atomic force microscope cantilevers. *Rev. Sci. Instrum.* 66:3789–3798.
22. Sader, J. E., J. A. Sanelli, …, E. J. Bieske. 2012. Spring constant calibration of atomic force microscope cantilevers of arbitrary shape. *Rev. Sci. Instrum.* 83:103705.
23. Sader, J. E., M. Yousefi, and J. R. Friend. 2014. Uncertainty in least-squares fits to the thermal noise spectra of nanomechanical resonators with applications to the atomic force microscope. *Rev. Sci. Instrum.* 85:025104.
24. Cappella, B., and G. Dietler. 1999. Force-distance curves by atomic force microscopy. *Surf. Sci. Rep.* 34:1–104.
25. Radmacher, M., M. Fritz, …, P. K. Hansma. 1996. Measuring the viscoelastic properties of human platelets with the atomic force microscope. *Biophys. J.* 70:556–567.
26. Grossmann, A., and J. Morlet. 1984. Decomposition of Hardy functions into square integrable wavelets of constant shape. *SIAM J. Math. Anal.* 15:723–736.
27. Y. Meyer, editor 1992. Wavelets and their Applications. Springer, Berlin, Germany.
28. Daubechies, I. 1992. Ten Lecture on Wavelets. SIAM, Philadelphia, PA.
29. Mallat, S. 1998. A Wavelet Tour of Signal Processing. Academic Press, New York.
30. Arneodo, A., B. Audit, …, C. Vaillant. 2002. Wavelet-based multifractal formalism: application to DNA sequences, satellite images of the cloud structure, and stock market data. *In* The Science of Disasters: Climate Disruptions, Heart Attacks, and Market Crashes. A. Bunde, J. Kropp, and H. J. Schellnhuber, editors. Springer, Berlin, Germany, pp. 26–102.
31. Arneodo, A., C. Vaillant, …, C. Thermes. 2011. Multi-scale coding of genomic information: from DNA sequence to genome structure and function. *Phys. Rep.* 498:45–188.
32. Roland, T., A. Khalil, …, F. Argoul. 2009. Revisiting the physical processes of vapodeposited thin gold films on chemically modified glass by atomic force and surface plasmon microscopies. *Surf. Sci.* 603:3307–3320.
33. Martinez-Torres, C., L. Berguiga, …, F. Argoul. 2014. Diffraction phase microscopy: retrieving phase contours on living cells with a wavelet-based space-scale analysis. *J. Biomed. Opt.* 19:36007.
34. Mallat, S., and W. L. Hwang. 1992. Singularity detection and processing with wavelets. *IEEE Trans. Inf. Theory.* 38:617–643.
35. Muzy, J. F., E. Bacry, and A. Arneodo. 1994. The multifractal formalism revisited with wavelets. *Int. J. Bifurcat. Chaos.* 4:245–302.
36. Delour, J., J. F. Muzy, and A. Arneodo. 2001. Intermittency of 1D velocity spatial profiles in turbulence: a magnitude cumulant analysis. *Eur. Phys. J. B.* 23:243–248.
37. Audit, B., E. Bacry, …, A. Arneodo. 2002. Wavelet-based estimators of scaling behavior. *IEEE Trans. Inf. Theory.* 48:2938–2954.
38. Arneodo, A., B. Audit, and P. Kestener. 2008. Wavelet-based multifractal analysis. *Scholarpedia.* 3:4103.
39. Domke, J., and M. Radmacher. 1998. Measuring the elastic properties of thin polymer films with the atomic force microscope. *Langmuir.* 14:3320–3325.
40. A-Hassan, E., W. F. Heinz, …, J. H. Hoh. 1998. Relative microelastic mapping of living cells by atomic force microscopy. *Biophys. J.* 74:1564–1578.
41. Crick, S. L., and F. C.-P. Yin. 2007. Assessing micromechanical properties of cells with atomic force microscopy: importance of the contact point. *Biomech. Model. Mechanobiol.* 6:199–210.
42. Carl, P., and H. Schillers. 2008. Elasticity measurement of living cells with an atomic force microscope: data acquisition and processing. *Pflugers Arch.* 457:551–559.
43. Gavara, N., and R. S. Chadwick. 2012. Determination of the elastic moduli of thin samples and adherent cells using conical atomic force microscope tips. *Nat. Nanotechnol.* 7:733–736.
44. Hertz, H. 1881. About the contact of solid elastic bodies [Über die berührung fester elastischer Körper]. *J. Reine Angew. Math.* 92:156–171.
45. Sneddon, I. N. 1965. The relation between load and penetration in the axisymmetric Boussinesq problem for a punch of arbitrary profile. *Int. J. Eng. Sci.* 3:47–57.
46. Rico, F., P. Roca-Cusachs, …, D. Navajas. 2005. Probing mechanical properties of living cells by atomic force microscopy with blunted pyramidal cantilever tips. *Phys. Rev. E Stat. Nonlin. Soft Matter Phys.* 72:021914.
47. Rosenbluth, M. J., W. A. Lam, and D. A. Fletcher. 2006. Force microscopy of nonadherent cells: a comparison of leukemia cell deformability. *Biophys. J.* 90:2994–3003.

48. Vella, D., A. Ajdari, …, A. Boudaoud. 2012. The indentation of pressurized elastic shells: from polymeric capsules to yeast cells. *J. R. Soc. Interface.* 9:448–455.

49. Vaziri, A., and A. Gopinath. 2008. Cell and biomolecular mechanics in silico. *Nat. Mater.* 7:15–23.

50. Gibson, L. J. 2012. The hierarchical structure and mechanics of plant materials. *J. R. Soc. Interface.* 9:2749–2766.

51. Geitmann, A. 2006. Plant and fungal cytomechanics: quantifying and modeling cellular architecture. *Can. J. Bot.* 84:1–13.

52. Beauzamy, L., N. Nakayama, and A. Boudaoud. 2014. Flowers under pressure: ins and outs of turgor regulation in development. *Ann. Bot. (Lond.).* 114:1517–1533.

53. Hayot, C. M., E. Forouzesh, …, J. A. Turner. 2012. Viscoelastic properties of cell walls of single living plant cells determined by dynamic nanoindentation. *J. Exp. Bot.* 63:2525–2540.

54. Fery, A., and R. Weinkamer. 2007. Mechanical properties of micro- and nanocapsules: single-capsule measurements. *Polymer (Guildf.).* 48: 7221–7235.